

A Search for Circumstellar Companions of Sirius B

MILES LUCAS ,¹ MICHAEL BOTTOM ,¹ GARRETH RUANE ,² AND SAM RAGLAND ,³

¹*Institute for Astronomy, University of Hawai'i, USA*

²*Jet Propulsion Laboratory, California Institute of Technology, USA*

³*W.M. Keck Observatory, USA*

ABSTRACT

We present deep imaging of Sirius B, the closest and brightest white dwarf. We use Keck/NIRC2 in L_p band (3.776 μm) across 3 epochs in 2020 using the technique of angular differential imaging. We reach sub-Jupiter sensitivities at sub-AU separations, down to an ultimate sensitivity of ∼0.6 M_J at ∼1.5 AU. Despite the high sensitivity of our observations, we do not detect any companions around Sirius B, which is consistent with previous studies. These observations showcase that for nearby faint targets direct imaging is ultimately limited by background noise more than contrast.

1. INTRODUCTION

High-contrast imaging (HCI) is a powerful technique for discovering and characterizing exoplanets. Being able to probe the architecture, formation, and atmospheres of planets directly is necessary for advancing substellar companion formation and evolution theory. The process required to image a planet is daunting, however. The typical astrophysical flux ratios for a Sun-Jupiter analog in the near-infrared (NIR) are ∼10⁻⁸, and for a Sun-Earth system are ∼10⁻¹⁰ (Traub & Oppenheimer 2010). In addition, the close angular separation of planets makes it difficult to detect them over the diffraction pattern of the star and other noise sources. In order to make such a difficult detection it is imperative to minimize diffraction, scattering, and systematic noise.

Typical targets for imaging are nearby young stars; the close proximity decreases the projected separation of the inner working angle (IWA) of the instrument, allowing closer investigation, and younger exoplanets are hotter and therefore the contrast is reduced. Another way to reduce contrast would be to reduce the luminosity of the star, which is not possible during the main-sequence (MS) lifetime of a star but is possible in the latest stages of stellar evolution. When intermediate mass stars (1 M_⊙ to 8 M_⊙) reach the end of their lifetimes, they become white dwarfs and begin cooling, which reduces their luminosity by a factor of 10³ – 10⁴ compared

to their progenitors. The faintness, broad spectral lines, and expanded orbits, as we will discuss below, all make white dwarfs exceptionally challenging for the transit photometry and radial velocity methods. However, the faintness reduces the contrast of planetary companions and the expanded separation greatly benefit imaging.

White dwarfs do present challenges, and there is limited knowledge of planetary systems around evolved stars. Burleigh et al. (2002); Veras (2016) suggests exoplanets on initially wide (>5 AU) orbits around intermediate mass stars will survive expansion during the red giant (RGB) phase. Furthermore, Nordhaus & Spiegel (2013) explain that close-in planets that escape the Roche limit of the expanding red giant can still be shredded by tidal forces, although the tidal forces on planets that readily escape engulfment are negligible. During the asymptotic giant (AGB) phase, stellar mass loss will adiabatically expand the orbit of the planet by a maximum factor of $M_{*,\text{MS}}/M_{*,\text{WD}}$ (Jeans 1924). Overall, the probability of discovering a *first-generation* planet around a white dwarf is low, but there are potential methods for *second-generation* planets to exist after the violent RGB and AGB phases.

The first search for substellar companions around white dwarfs was conducted by Probst (1983) by looking for infrared (IR) excess in their spectral energy distributions (SED) using broadband photometry. This excess could likely be attributed to circumstellar dust or gas discs, which are indicators of the planetary formation history. Of the ∼100 white dwarfs they studied, no companions were found. The same method was applied by Zuckerman & Becklin (1987) who found excess IR emission around white dwarf G29-38. Eventually this

excess was determined to be from a dust disc (Telesco et al. 1990), with the current interpretation associating the dust with accretion onto the white dwarf, polluting the stellar atmosphere (Koester et al. 1997).

To date, there has been no direct images of an exoplanet around a white dwarf. The only planetary-mass object imaged around a single white dwarf (WD 0806-661B) was discovered using Spitzer with a mass of $7 M_J$ on a wide 2500 AU orbit (Luhman et al. 2011). The “Degenerate Objects around Degenerate Objects” survey (DODO; Hogan et al. 2009) observed 29 white dwarfs with Gemini/NIRI and VLT/ISAAC, reaching an average upper limit around $\sim 8 M_J$ beyond 35 AU. The young white dwarf GD 50 was observed using the extreme AO instrument SPHERE at the VLT (Xu et al. 2015), reaching sensitivity limits of $4 M_J$ at 6.2 AU.

A particularly fascinating white dwarf is Sirius B, the closest and brightest white dwarf. The Sirius system is the 7th closest to the sun at 2.6 pc, consisting of Sirius A, a -1.35 magnitude A1Vm star known for being the brightest, and Sirius B, a DA2 white dwarf with a 50 yr orbit (Bond et al. 2017; Gaia Collaboration et al. 2018). As mentioned previously, the proximity and faintness of Sirius B (compared to a MS star) make it compelling for imaging, and additionally it is a young system (~ 225 Myr), further reducing the predicted contrast necessary to image a planetary companion.

The orbit of Sirius B was first studied by Bessel (1844), who recognized wobbles in the proper motion of Sirius A caused by a “dark satellite”. This dark satellite was visually confirmed in Bond (1862) as Sirius B. Adams (1915) took the first spectral measurements of Sirius B and found it to be similar to a MS early A-type star, despite its faintness, which we now know to be typical of white dwarf spectra.

Initial astrometric perturbations suggested a 50 year orbital period (Auwers 1864), with the first orbital solution including dynamic masses published by van den Bos (1960). Gatewood & Gatewood (1978) improved upon the van den Bos orbital solution with over 300 more images, finding nearly the same dynamical masses for the binary. Bond et al. (2017) greatly refined the orbit using a compilation of historical data and Hubble Space Telescope (HST) data, which gave dynamical masses of $(2.063 \pm 0.023) M_\odot$ and $(1.018 \pm 0.011) M_\odot$ for A and B, respectively.

The precise dynamical masses are key for finding the age of Sirius; Bond et al. (2017) report a cooling age for Sirius B of 126 Myr using isochrones. Studies of the initial-final mass relation (IFMR) of white dwarfs (Cummings et al. 2016) lead to estimates of the progenitor mass of Sirius B to be between $5 M_\odot$ to $5.6 M_\odot$, which,

when combined with stellar evolution codes, yield total ages between 226 Myr to 228 Myr with an uncertainty of about ± 10 Myr (Bond et al. 2017). The precision of the system age is useful for constraining the mass of potential companions.

A companion around Sirius B would be affected by the orbit of Sirius A, and this constrained three-body system has been studied numerically (Holman & Wiegert 1999). Bond et al. (2017) calculate the longest period stable companion around Sirius B is 1.79 yr, which corresponds to a 1.5 AU circular orbit.

Some of the first modern imaging studies searching for companions around Sirius B were Schroeder et al. (2000) and Kuchner & Brown (2000), who used the HST planetary camera and NICMOS cameras, respectively, looking for signal around 1 μm , which combined had a sensitivity down to $\sim 10 M_J$ at 2'' (5.3 AU). Bonnet-Bidaud & Pantin (2008) use the ground-based ESO/ADONIS instrument in JHKs to reach a sensitivity of $\sim 30 M_J$ at 3'' (7.9 AU). Skemer & Close (2011) used mid-IR (out to 10 μm) observations from Gemini/T-ReCs which ruled out evidence for any infrared excess around Sirius B. Thalmann et al. (2011) use Subaru/IRCS at 4.05 μm reaching detection sensitivities of $6 M_J$ to $12 M_J$ at 1''. Recently, Pathak et al. (2021) took simultaneous mid-IR observations (10 μm) at VLT/VISIR of Sirius A (through a coronagraph) and B. Because of the simultaneous observation, their contrast depended on which region of the FOV was tested. Their average sensitivity is $\sim 2.5 M_J$ at 1 AU, and their best sensitivity (from the “inner” region) is $\sim 1.5 M_J$ at 1 AU.

In this work we report our study of Sirius B using direct images from Keck/NIRC2. section 2 describes our target and observing strategy, section 3 describes the processing and analysis techniques used, section 4 describes our results and we conclude with section 5.

2. OBSERVATIONS

Despite Sirius B being the brightest white dwarf in the sky, it is still 10 magnitudes fainter than Sirius A, making it a technically challenging target, especially on ground-based telescopes which have to deal with extra scattering and diffraction from the atmosphere.

We targeted Sirius B directly using Keck/NIRC2 in Lp-band (3.776 μm) across three epochs in 2020 (Table 1). Our first attempt to observe Sirius B failed due to the strong scattered light from Sirius A. The adaptive optics (AO) calibration failed when the -1.35 K-band magnitude diffraction patterns from Sirius A would sweep into the field of view (FOV) of the wavefront sensor (WFS). Similarly, trying to deploy the focal-plane vortex coronagraph (Serabyn et al. 2017) failed when

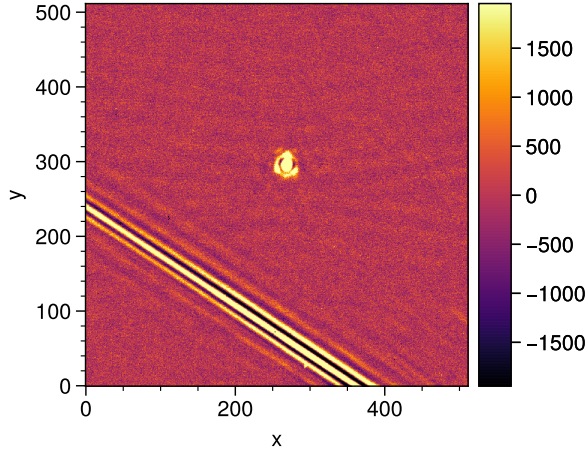


Figure 1. Calibrated science frame of Sirius b from 2020-02-04 epoch showing the strong scattered light effects from Sirius a.

the coronagraphic pointing control algorithm, QACITS (Huby et al. 2017), performed erratically in the presence of the scattered light. Vigan et al. (2015, §2) reported similar issues in their attempts to image Sirius B. In order to overcome these obstacles, we decided to try using Sirius A as the AO guide star and off-axis guiding to Sirius B.

The Keck AO system (Wizinowich et al. 2000) was not designed to accommodate stars as bright as Sirius A, so we needed to attenuate the flux greatly to avoid saturating the WFS. We experimented with different filters in front of the WFS, settling on a narrow laser-line filter which attenuated Sirius B by ~ 6 magnitudes. While still bright (appearing like a ~ 5 magnitude star on the WFS), this was enough attenuation to close the AO loop. From here, we slewed off-axis using the separations and position angles calculated in Table 1 from the orbital parameters in Bond et al. (2017). In this mode, we noticed higher than usual drift in the focal plane, requiring manually recentering the target every 5 or 10 minutes. We tried deploying the vortex coronagraph along with QACITS, but again the scattered light from Sirius A made QACITS unstable, so we decided to forego any coronagraphy for the remaining observations.

During each observation, we took calibration frames in the form of dark frames and sky flat frames. We also disabled the field rotator, which caused the FOV to rotate throughout the night for angular differential imaging (ADI; Marois et al. 2006).

3. ANALYSIS

For each epoch we applied a flat correction using calibration frames captured during observing. We also removed bad pixels using a combination of L.A.Cosmic (van Dokkum 2001) and an adaptive sigma-clipping algorithm. We removed sky background using a high-pass median filter with a box size of 31 pixels. For both the November epochs we tried exploiting the large focal plane drifts by dithering between two positions in order to simplify background subtraction, but this ended up performing worse than the high-pass filter. At this point frames were manually selected to remove bad frames, especially those with diffraction spikes from Sirius A within a few hundred pixels, like in Figure 1. Then, each good frame was co-registered to sub-pixel accuracy using the algorithm presented in Guizar-Sicairos et al. (2008), followed by fitting each frame with a Gaussian PSF. The co-registered frames are then shifted to the center of the FOV. Lastly the frames were cropped to the inner 200 pixels and stacked into data cubes for each epoch. With the pixel scale of 10 mas/px the crop corresponds to a maximum separation of $1''$ or a projected separation of 2.7 AU. We also measure the parallactic angle of each frame, including corrections for distortion effects following Yelda et al. (2010). For each epoch, we measure the full-width at half-maximum (FWHM) of the stellar PSF by fitting a bivariate Gaussian model to the median frame from each data cube (Figure 2). All of the pre-processing code is available in Jupyter notebooks at the following GitHub repository¹ and the pre-processed data cubes and parallactic angles are available on Zenodo (Lucas et al. 2021).

By taking data with the field rotator disabled (ADI), the point-spread function (PSF) will not appear to rotate while any potential companion will appear to rotate. This reduces the probability of subtracting companion signal when we subtract the stellar PSF model. After subtraction, the frames are derotated by their parallactic angle and combined with a weighted sum (Bottom et al. 2017), which reduces the pixel-to-pixel noise as the number of frames in the data cube increases.

For this analysis we used four ADI algorithms for modeling and subtracting the stellar PSF: median subtraction (Marois et al. 2006), principal component analysis (PCA, also referred to as KLIP; Soummer et al. 2012), non-negative matrix factorization (NMF; Ren et al. 2018), and fixed-point greedy disk subtraction (GreeDS; Pairet et al. 2019b, 2020). The median subtraction and PCA methods were also applied in an annular method, where we modeled the PSF in annuli of

¹ <https://github.com/mileslucas/sirius-b>

Table 1. Observing parameters for the three epochs of data. All observations were carried out using the NIRC2 Lp-band filter. Observation time is based on the frames that were selected for processing.

| Date observed | Sirius B offset (") | Sirius B PA (°) | Obs. time (hr) | FOV rotation (°) | FWHM (mas) | Seeing (") | Temp (°C) | PWV (mm) |
|---------------|---------------------|-----------------|----------------|------------------|------------|------------|-----------|----------|
| 2020-02-04 | 11.20 | 67.90 | 1.44 | 60.1 | 79.9 | | | |
| 2020-11-21 | 11.27 | 66.42 | 2.91 | 91.4 | 76.4 | | | |
| 2020-11-28 | 11.27 | 66.38 | 2.44 | 80.4 | 82.2 | | | |

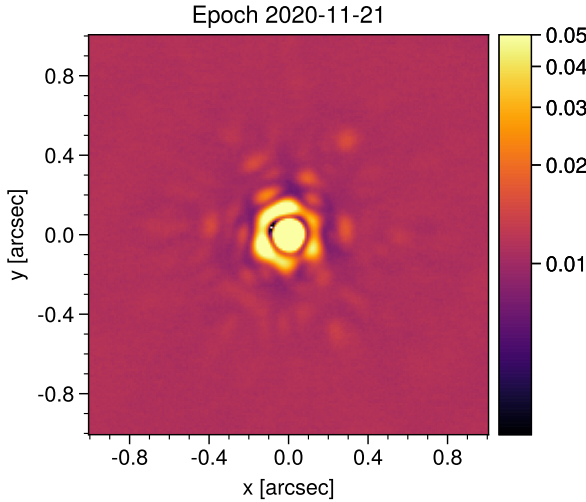


Figure 2. The median frame from the 2020-11-21 epoch showing the instrumental PSF. The inner core has a FWHM of ~ 76 mas. The speckle pattern is shown in the blobs surrounding the first ring, with roughly 6-way radial symmetry corresponding to the hexagonal shape of the primary mirror.

increasing separation frame-by-frame, discarding frames which have not rotated at least 0.5 FWHM (Marois et al. 2006).

We used three metrics for determining the performance of each algorithm, the signal-to-noise ratio (S/N) significance map, the standardized trajectory intensity mean map (STIM map; Pairet et al. 2019a), and the contrast curve. The significance and STIM maps assign a likelihood to each pixel for the presence of a companion using different assumptions of the residual statistics. The contrast curve determines the sensitivity of a 5σ statistical detection through repeated injection and retrieval of planetary signal as processed by one of the ADI algorithms above. We calculate both the Gaussian contrast and the Student-t corrected contrast, which accounts for the small-sample statistics in each annulus (Mawet et al. 2014). The collapsed residual frames along with the above metrics for each algorithm for each epoch are in Appendix A.

A common problem when using subspace-driven ADI algorithms like PCA, NMF, or GreeDS is choosing the size of the subspace (i.e., the number of components). In our analysis we employ the STIM largest intensity mask map (SLIM map; Pairet 2020) as an ensemble statistic. The SLIM map calculates the average STIM map from many residual cubes along with the average mask of the N most intense pixels in each STIM map. A real companion ought to be present in many different residual cubes from the same dataset, so this ensemble approach can give us a probability map without having to settle on the number of components ahead of time. For PCA, NMF, and GreeDS algorithms, we created residual cubes for increasing number of components, from 1 to 10. We chose 10 as the max number of components because we saw a dramatic dropoff in contrast sensitivity after the first few components. The collapsed residual frames, average STIM map, SLIM map, and contrast curves for each epoch for each of the above algorithms can be found in Appendix A.

All of the ADI algorithms and metrics are implemented in the open-source Julia package ADI.jl (Lucas & Bottom 2020). All of the code for the ADI processing in this paper, including the scripts for each figure produced are in a GitHub repository² in Jupyter notebooks and Julia scripts.

4. RESULTS

We determined the best-performing algorithms for each epoch using the contrast curves described in section 3. For the first two epochs full-frame median subtraction had the best contrast at all separations. For the last epoch annular PCA subtraction with 2 principal components and a rotation threshold of 0.5 FWHM produced the best contrast at close separations ($0.2''$ to $0.4''$) and had similar performance to other algorithms beyond $0.4''$. The collapsed residual frames from each epoch are shown in Figure 3, along with the Gaussian significance maps (Figure 4) and STIM maps (Figure 5).

² <https://github.com/mileslucas/sirius-b>

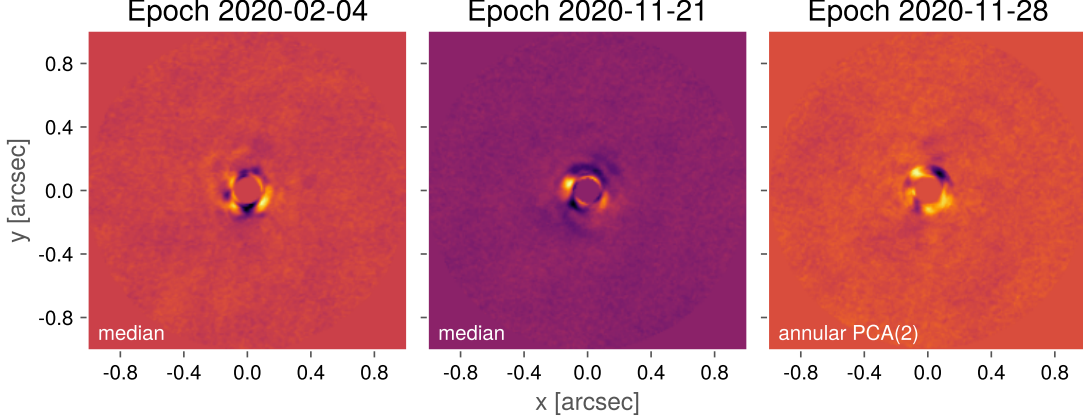


Figure 3. The flat residuals of each epoch after PSF subtraction, derotating, and collapsing. The inner full-width at half-maximum (FWHM) is masked out for each frame.

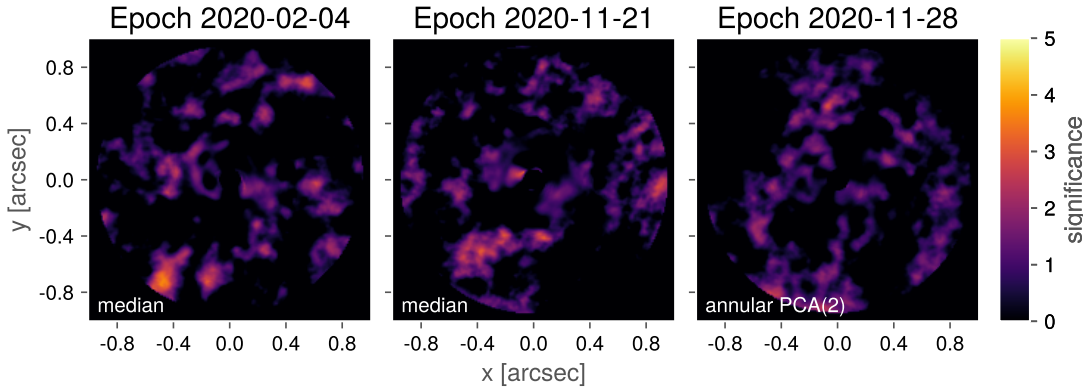


Figure 4. The *significance* maps for each epoch accounting for small sample statistics (Mawet et al. 2014). Typically a critical value for detection is 5. The inner full-width at half-maximum (FWHM) is masked out for each map.

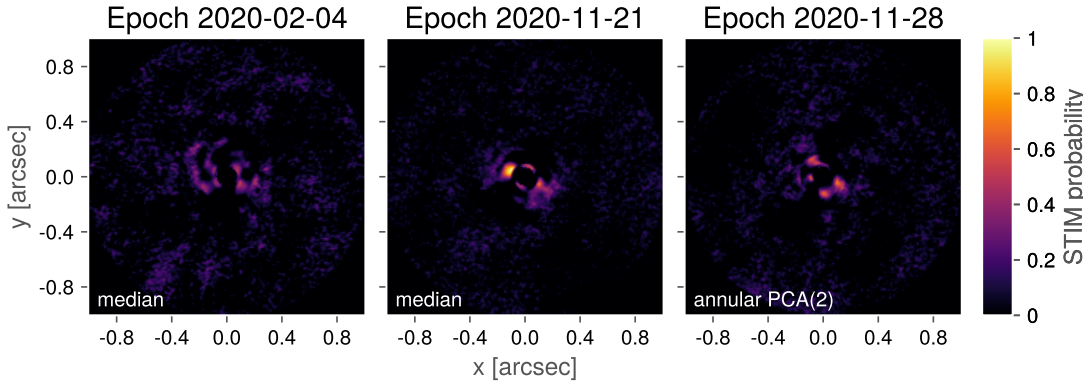


Figure 5. The STIM maps for each epoch calculated from the residual cube. The STIM probability has a typical cutoff threshold of 0.5 for significant detections. The inner full-width at half-maximum (FWHM) is masked out for each map.

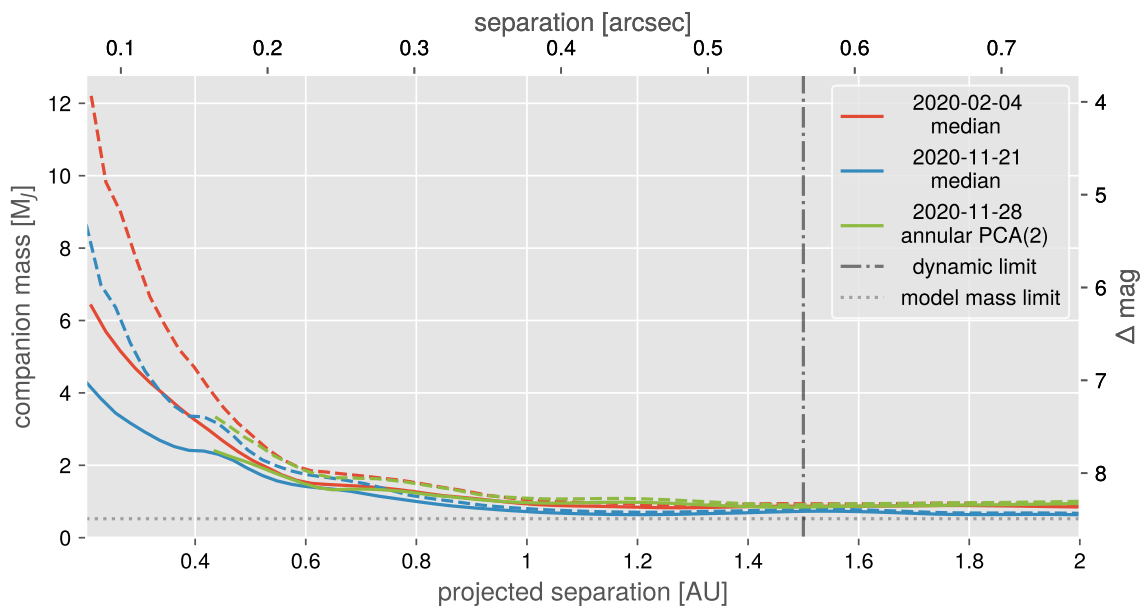


Figure 6. The contrast curves for the best performing algorithm from each epoch. The solid lines are the Gaussian 5σ contrast curves and the dashed lines are the Student-t corrected curves. In addition, the expected upper limit for orbital separation of a stable orbit of 1.5 AU is plotted as a vertical dashed line. The companion mass values are interpolated from the AMES-Cond grid. The lower mass limit (upper magnitude limit) of these models is plotted in a light-gray horizontal dashed line.

In these images there is not *consistent* or overwhelming evidence for a substellar companion. The STIM probability maps for the 2020-11-21 and 2020-11-28 epochs suggest evidence for some blobs $\sim 0.13''$ from the center. The lack of evidence in the February epoch and the significance maps as well as the proximity to the central star (~ 2 FWHM) all reduce the probability of these blobs being true companions. Nonetheless, we estimated astrometry for blobs from each epoch (Table 2) and tried fitting Keplerian orbits using the “Orbits for the Impatient” algorithm (OFTI; Blunt et al. 2017). We generated 10^4 orbits, none of which managed to contain the points from each epoch (Appendix B). We take this as direct evidence against the blobs being substellar companions of any kind.

It is interesting to note the morphology of the innermost $\sim 0.4''$ in the frames produced by GreeDS and NMF. Both of these algorithms outperform traditional median and PCA subtraction for disk imaging. In the frames from each epoch, but particularly in the two November epochs, a symmetric “barbell” shape can be seen. Due to the nature of high-contrast imaging, it is difficult to differentiate systematic noise from real signal in the speckle-limited regime, in addition there is no prior evidence for a circumstellar disk from IR excess. Follow-up work in the visible (e.g., Subaru/VAMPIRES, VLT/SPHERE) may be able to image such a disk.

The contrast maps from the best performing algorithm for each reduction are shown in Figure 6. We determine the limiting sensitivities in terms of the planetary mass by first calculating the contrast-limited magnitude using an Lp-band magnitude for Sirius B of 9.1 (adapted from Bonnet-Bidaud & Pantin 2008). Then we use an age of 226 Myr to interpolate the planetary mass using the AMES-Cond evolutionary grid and atmosphere models (Allard et al. 2012). It is important to note how the precision of the system age (see section 1) reduces uncertainty when interpolating planetary mass from the evolutionary grids. The best performing epoch was on the night of 2020-11-21, which managed to reach an exceptional sensitivity of $3.5 M_J$ at $0.25 AU$ ($0.09''$)

in the speckle limited regime and ultimately $0.6 M_J$ at $1.5 AU$ ($0.38''$) in the sky-background limited regime.

5. CONCLUSIONS

In closing, the Sirius system is one of the most well studied in history, with Sirius B being the target of companion searches from the visible to the IR. While it is highly unlikely a first-generation planet survived post-MS evolution, imaging efforts have gradually increased the sensitivity to second-generation planets. In this work we present high-contrast images of Sirius B in the near-IR. Our sensitivity limits are the best that have been reached for Sirius B, reaching $3.5 M_J$ at $0.25 AU$. In the mid-IR previous works have only probed as close-in as $\sim 1 AU$, where we reach a sensitivity of $0.72 M_J$. Despite the high sensitivity of this study, we found no appreciable evidence for a companion around Sirius B, consistent with previous results.

In recent years improving contrast and inner working angle were the dominant parameters of interest. Our observations here show that for nearby faint targets (white dwarfs, M-dwarfs, etc.) we are limited more by the sky background than the speckle noise. Our sensitivities reach the background limit at $\sim 0.4''$, which would correspond to projected separations of $1 AU$ to $10 AU$ for stars at $2.7 pc$ to $25 pc$. This means we could potentially reach sub-Jupiter sensitivities for 10s-100s of targets without coronagraphy.

We have published alongside this work the entire codebase used for pre-processing and reducing the data, and for generating every figure in this manuscript. We have also published our reduced datasets under an open license. We hope that this improves the reproducibility of the work as well as providing data for exploring new and different ADI algorithms.

Software: ADI.jl (Lucas & Bottom 2020), astropy (Collaboration et al. 2013; Astropy Collaboration et al. 2018), Julia (Bezanson et al. 2017), numpy (Harris et al. 2020), scikit-image (Walt et al. 2014),

REFERENCES

- Adams, W. S. 1915, Publications of the Astronomical Society of the Pacific, 27, 236, doi: [10.1086/122440](https://doi.org/10.1086/122440)
- Allard, F., Homeier, D., & Freytag, B. 2012, Philos Trans A Math Phys Eng Sci, 370, 2765, doi: [10.1098/rsta.2011.0269](https://doi.org/10.1098/rsta.2011.0269)
- Astropy Collaboration, Price-Whelan, A. M., Sipőcz, B. M., et al. 2018, The Astronomical Journal, 156, 123, doi: [10.3847/1538-3881/aabc4f](https://doi.org/10.3847/1538-3881/aabc4f)
- Auwers, A. 1864, Monthly Notices of the Royal Astronomical Society, 25, 38. <https://ui.adsabs.harvard.edu/abs/1864MNRAS..25...38A>

- Bessel, F. W. 1844, Monthly Notices of the Royal Astronomical Society, 6, 136, doi: [10.1093/mnras/6.11.136](https://doi.org/10.1093/mnras/6.11.136)
- Bezanson, J., Edelman, A., Karpinski, S., & Shah, V. B. 2017, SIAM Rev., 59, 65, doi: [10.1137/141000671](https://doi.org/10.1137/141000671)
- Blunt, S., Nielsen, E. L., De Rosa, R. J., et al. 2017, The Astronomical Journal, 153, 229, doi: [10.3847/1538-3881/aa6930](https://doi.org/10.3847/1538-3881/aa6930)
- Bond, G. 1862, Astronomische Nachrichten, 57, 131. <https://ui.adsabs.harvard.edu/abs/1862AN.....57..131B>
- Bond, H. E., Schaefer, G. H., Gilliland, R. L., et al. 2017, The Astrophysical Journal, 840, 70, doi: [10.3847/1538-4357/aa6af8](https://doi.org/10.3847/1538-4357/aa6af8)
- Bonnet-Bidaud, J.-M., & Pantin, E. 2008, A&A, 489, 651, doi: [10.1051/0004-6361:20078937](https://doi.org/10.1051/0004-6361:20078937)
- Bottom, M., Ruane, G., & Mawet, D. 2017, Research Notes of the American Astronomical Society, 1, 30, doi: [10.3847/2515-5172/aa9d18](https://doi.org/10.3847/2515-5172/aa9d18)
- Burleigh, M. R., Clarke, F. J., & Hodgkin, S. T. 2002, Monthly Notices of the Royal Astronomical Society, 331, L41, doi: [10.1046/j.1365-8711.2002.05417.x](https://doi.org/10.1046/j.1365-8711.2002.05417.x)
- Collaboration, A., Robitaille, T. P., Tollerud, E. J., et al. 2013, Astronomy and Astrophysics, 558, A33, doi: [10.1051/0004-6361/201322068](https://doi.org/10.1051/0004-6361/201322068)
- Cummings, J. D., Kalirai, J. S., Tremblay, P. E., & Ramirez-Ruiz, E. 2016, The Astrophysical Journal, 818, 84, doi: [10.3847/0004-637X/818/1/84](https://doi.org/10.3847/0004-637X/818/1/84)
- Gaia Collaboration, Brown, A. G. A., Vallenari, A., et al. 2018, Astronomy & Astrophysics, Volume 616, id.A1, <NUMPAGES>22</NUMPAGES> pp., 616, A1, doi: [10.1051/0004-6361/201833051](https://doi.org/10.1051/0004-6361/201833051)
- Gatewood, G. D., & Gatewood, C. V. 1978, The Astrophysical Journal, 225, 191, doi: [10.1086/156480](https://doi.org/10.1086/156480)
- Guizar-Sicairos, M., Thurman, S. T., & Fienup, J. R. 2008, Opt. Lett., OL, 33, 156, doi: [10.1364/OL.33.000156](https://doi.org/10.1364/OL.33.000156)
- Harris, C. R., Millman, K. J., van der Walt, S. J., et al. 2020, Nature, 585, 357, doi: [10.1038/s41586-020-2649-2](https://doi.org/10.1038/s41586-020-2649-2)
- Hogan, E., Burleigh, M. R., & Clarke, F. J. 2009, Monthly Notices of the Royal Astronomical Society, 396, 2074, doi: [10.1111/j.1365-2966.2009.14565.x](https://doi.org/10.1111/j.1365-2966.2009.14565.x)
- Holman, M. J., & Wiegert, P. A. 1999, The Astronomical Journal, 117, 621, doi: [10.1086/300695](https://doi.org/10.1086/300695)
- Huby, E., Baudoz, P., Mawet, D., & Absil, O. 2017, The Astronomical Journal, 153, 43, doi: [10.3847/1538-3881/153/1/43](https://doi.org/10.3847/1538-3881/153/1/43)
- Jeans, J. H. 1924, Monthly Notices of the Royal Astronomical Society, 85, 2, doi: [10.1093/mnras/85.1.2](https://doi.org/10.1093/mnras/85.1.2)
- Koester, D., Provencal, J., & Shipman, H. L. 1997, Astronomy and Astrophysics, v.320, p.L57-L59, 320, L57. <https://ui.adsabs.harvard.edu/abs/1997A%26A...320L..57K/abstract>
- Kuchner, M. J., & Brown, M. E. 2000, Publications of the Astronomical Society of the Pacific, 112, 827, doi: [10.1086/316581](https://doi.org/10.1086/316581)
- Lucas, M., & Bottom, M. 2020, Journal of Open Source Software, 5, 2843, doi: [10.21105/joss.02843](https://doi.org/10.21105/joss.02843)
- Lucas, M., Bottom, M., Ruane, G., & Ragland, S. 2021, NIRC2 Sirius b ADI data, Zenodo, doi: [10.5281/zenodo.5115225](https://doi.org/10.5281/zenodo.5115225)
- Luhman, K. L., Burgasser, A. J., & Bochanski, J. J. 2011, The Astrophysical Journal, 730, L9, doi: [10.1088/2041-8205/730/1/L9](https://doi.org/10.1088/2041-8205/730/1/L9)
- Marois, C., Lafrenière, D., Doyon, R., Macintosh, B., & Nadeau, D. 2006, The Astrophysical Journal, 641, 556, doi: [10.1086/500401](https://doi.org/10.1086/500401)
- Mawet, D., Milli, J., Wahhaj, Z., et al. 2014, ApJ, 792, 97, doi: [10.1088/0004-637X/792/2/97](https://doi.org/10.1088/0004-637X/792/2/97)
- Nordhaus, J., & Spiegel, D. S. 2013, Monthly Notices of the Royal Astronomical Society, 432, 500, doi: [10.1093/mnras/stt569](https://doi.org/10.1093/mnras/stt569)
- Pairet, B. 2020, PhD thesis, UCL - Université Catholique de Louvain. <https://dial.uclouvain.be/pr/boreal/object/boreal:240621>
- Pairet, B., Cantalloube, F., Gomez Gonzalez, C. A., Absil, O., & Jacques, L. 2019a, Monthly Notices of the Royal Astronomical Society, 487, 2262, doi: [10.1093/mnras/stz1350](https://doi.org/10.1093/mnras/stz1350)
- Pairet, B., Cantalloube, F., & Jacques, L. 2019b, arXiv:1812.01333 [astro-ph]. <http://arxiv.org/abs/1812.01333>
- . 2020, arXiv:2008.05170 [astro-ph]. <http://arxiv.org/abs/2008.05170>
- Pathak, P., de la Roche, D. J. M. P. d., Kasper, M., et al. 2021, arXiv:2104.13032 [astro-ph]. <http://arxiv.org/abs/2104.13032>
- Probst, R. G. 1983, The Astrophysical Journal Supplement Series, 53, 335, doi: [10.1086/190893](https://doi.org/10.1086/190893)
- Ren, B., Pueyo, L., Zhu, G. B., Debes, J., & Duchêne, G. 2018, The Astrophysical Journal, 852, 104, doi: [10.3847/1538-4357/aa1f2](https://doi.org/10.3847/1538-4357/aa1f2)
- Schroeder, D. J., Golimowski, D. A., Brukardt, R. A., et al. 2000, The Astronomical Journal, 119, 906, doi: [10.1086/301227](https://doi.org/10.1086/301227)
- Serabyn, E., Huby, E., Matthews, K., et al. 2017, The Astronomical Journal, 153, 43, doi: [10.3847/1538-3881/153/1/43](https://doi.org/10.3847/1538-3881/153/1/43)

- Skemer, A. J., & Close, L. M. 2011, The Astrophysical Journal, 730, 53, doi: [10.1088/0004-637X/730/1/53](https://doi.org/10.1088/0004-637X/730/1/53)
- Soummer, R., Pueyo, L., & Larkin, J. 2012, The Astrophysical Journal Letters, 755, L28, doi: [10.1088/2041-8205/755/2/L28](https://doi.org/10.1088/2041-8205/755/2/L28)
- Telesco, C. M., Joy, M., & Sisk, C. 1990, The Astrophysical Journal, 358, L17, doi: [10.1086/185769](https://doi.org/10.1086/185769)
- Thalmann, C., Usuda, T., Kenworthy, M., et al. 2011, The Astrophysical Journal, 732, L34, doi: [10.1088/2041-8205/732/2/L34](https://doi.org/10.1088/2041-8205/732/2/L34)
- Traub, W. A., & Oppenheimer, B. R. 2010, Exoplanets, 111. <http://adsabs.harvard.edu/abs/2010exop.book..111T>
- van den Bos, W. H. 1960, Journal des Observateurs, 43, 145. <https://ui.adsabs.harvard.edu/abs/1960JO.....43..145V>
- van Dokkum, P. G. 2001, Publications of the Astronomical Society of the Pacific, 113, 1420, doi: [10.1086/323894](https://doi.org/10.1086/323894)
- Veras, D. 2016, Royal Society Open Science, 3, 150571, doi: [10.1098/rsos.150571](https://doi.org/10.1098/rsos.150571)
- Vigan, A., Gry, C., Salter, G., et al. 2015, Monthly Notices of the Royal Astronomical Society, 454, 129, doi: [10.1093/mnras/stv1928](https://doi.org/10.1093/mnras/stv1928)
- Walt, S. v. d., Schönberger, J. L., Nunez-Iglesias, J., et al. 2014, PeerJ, 2, e453, doi: [10.7717/peerj.453](https://doi.org/10.7717/peerj.453)
- Wizinowich, P. L., Acton, D. S., Lai, O., et al. 2000, 4007, 2, doi: [10.1117/12.390368](https://doi.org/10.1117/12.390368)
- Xu, S., Ertel, S., Wahhaj, Z., et al. 2015, Astronomy & Astrophysics, Volume 579, id.L8, <NUMPAGES>5</NUMPAGES> pp., 579, L8, doi: [10.1051/0004-6361/201526179](https://doi.org/10.1051/0004-6361/201526179)
- Yelda, S., Lu, J. R., Ghez, A. M., et al. 2010, The Astrophysical Journal, Volume 725, Issue 1, pp. 331-352 (2010)., 725, 331, doi: [10.1088/0004-637X/725/1/331](https://doi.org/10.1088/0004-637X/725/1/331)
- Zuckerman, B., & Becklin, E. E. 1987, Nature, 330, 138, doi: [10.1038/330138a0](https://doi.org/10.1038/330138a0)

APPENDIX

A. ADI PROCESSING RESULTS

Results from processing each epoch of Sirius B data with various ADI algorithms. The top-left image is the subtracted, derotated, and collapsed image. The top-middle image is the Gaussian S/N map, the bottom-middle image is the Student-t S/N (significance) map, which typically requires a value of 5 to show a significant detection, and the bottom-left image is the STIM probability map, which typically requires a probability of 0.5 for significant detection. The right graph shows the 5σ contrast, both the Gaussian and Student-t corrected curves.

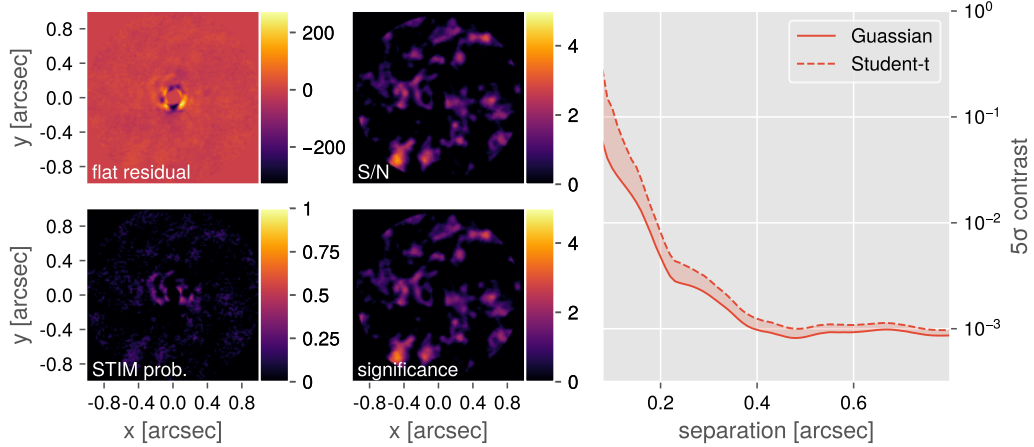


Figure 7. 2020-02-04 median

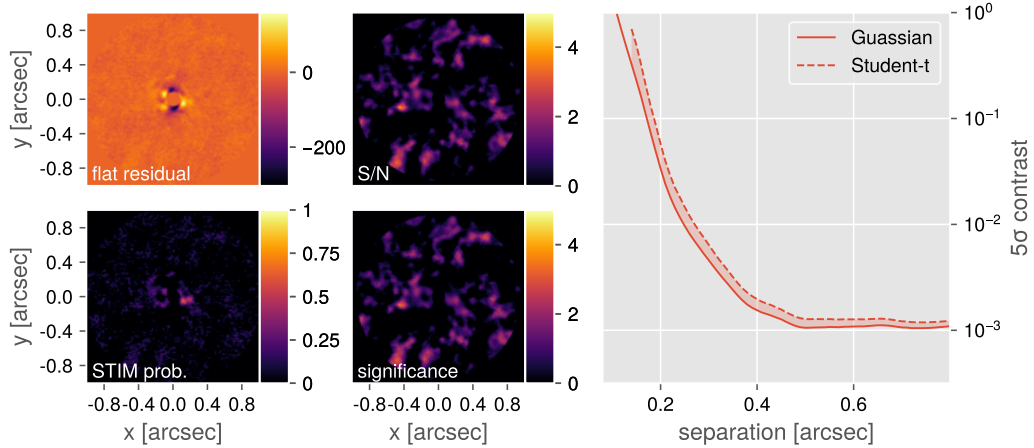


Figure 8. 2020-02-04 PCA(2)

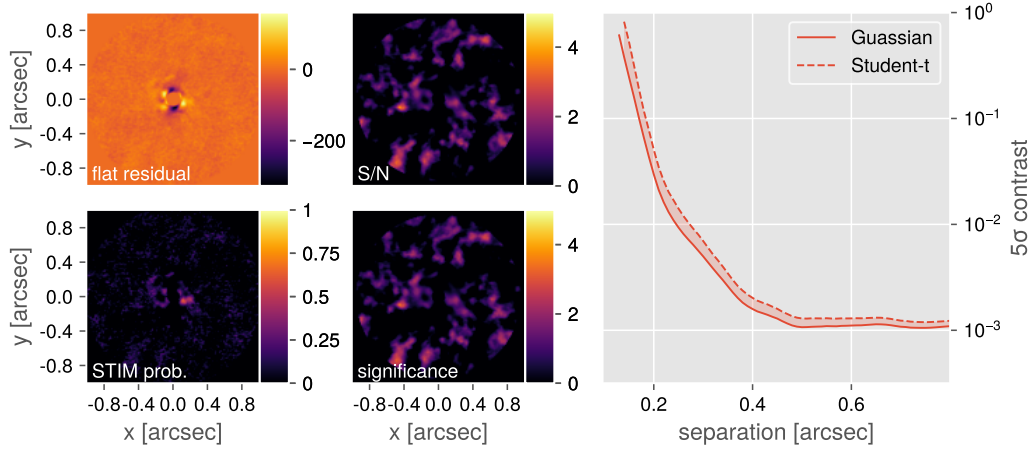


Figure 9. 2020-02-04 NMF(2))

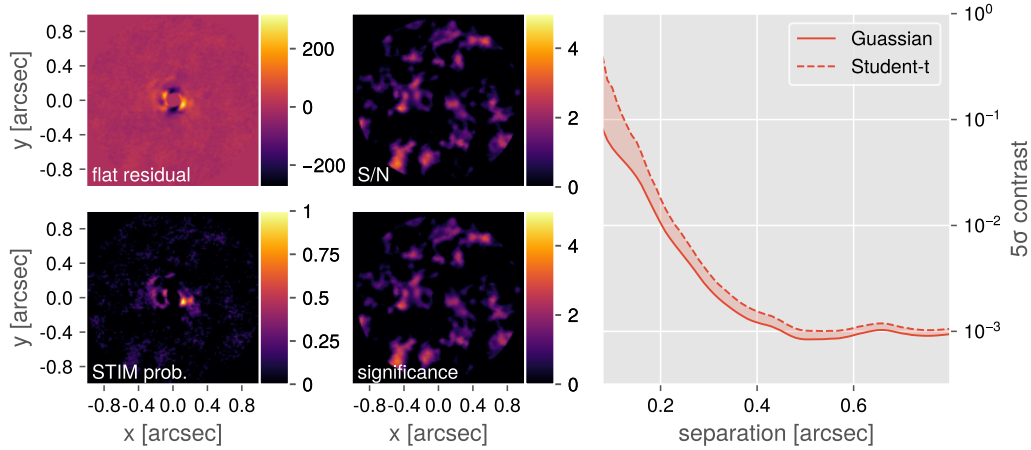


Figure 10. 2020-02-04 GreeDS(2)

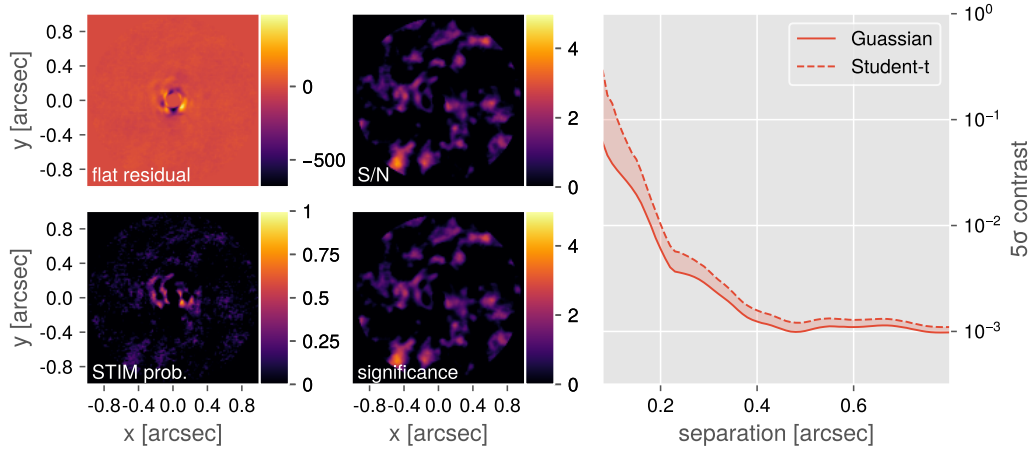


Figure 11. 2020-02-04 annular median

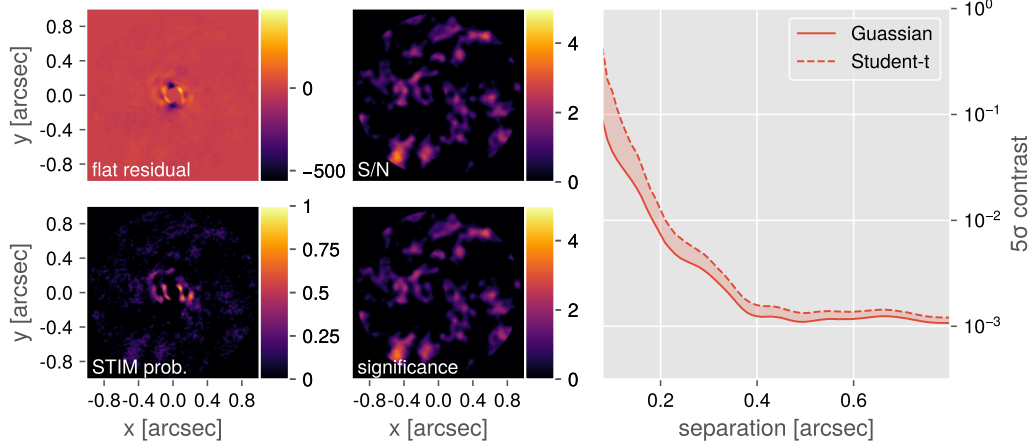


Figure 12. 2020-02-04 annular PCA(2))

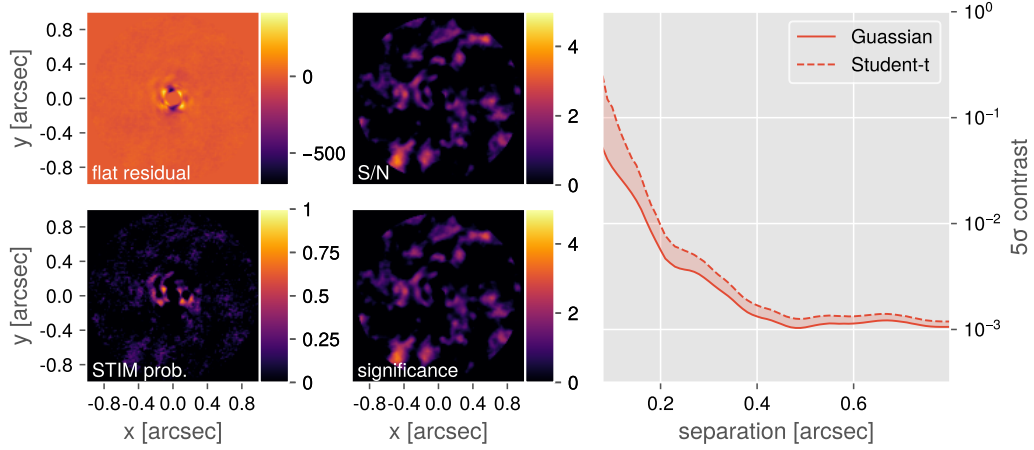


Figure 13. 2020-02-04 annular NMF(2)

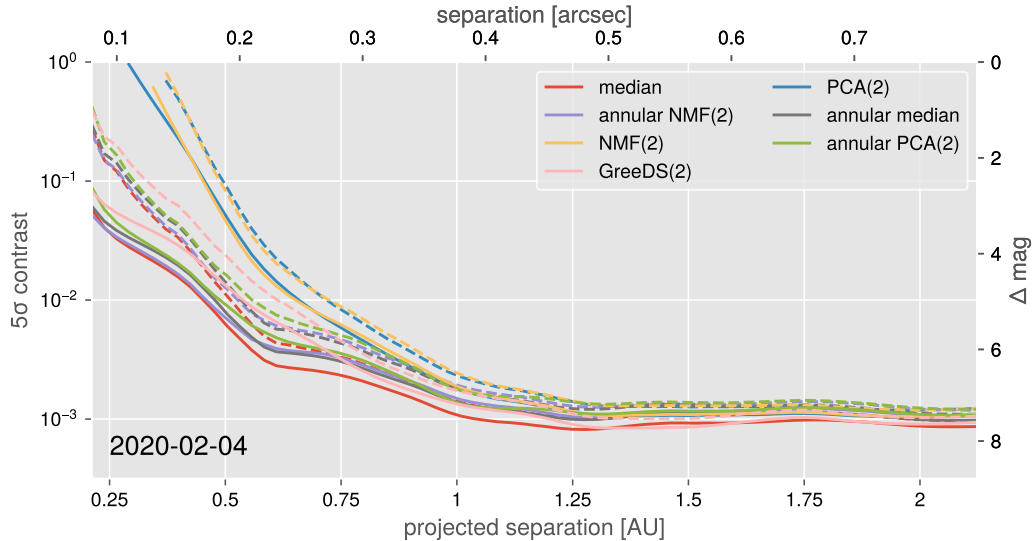


Figure 14. 5σ contrast curves from various ADI algorithms for the 2020-02-04 epoch. Both the Gaussian (solid lines) and Student-t corrected (dashed lines) contrast curves are shown.

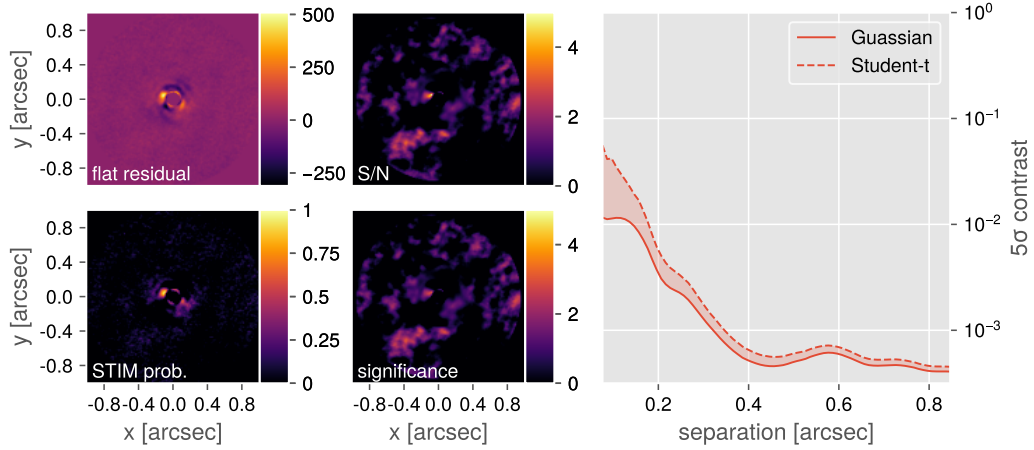


Figure 15. 2020-11-21 median subtraction.

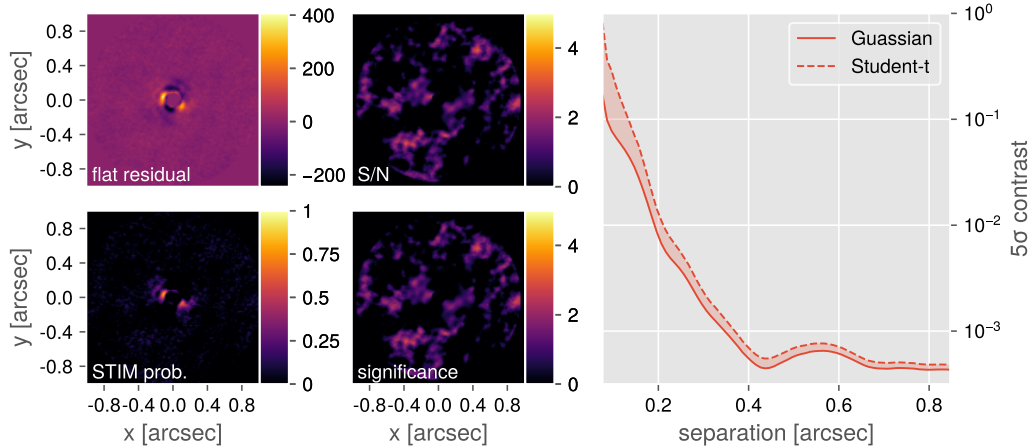


Figure 16. 2020-11-21 PCA subtraction with 2 components.

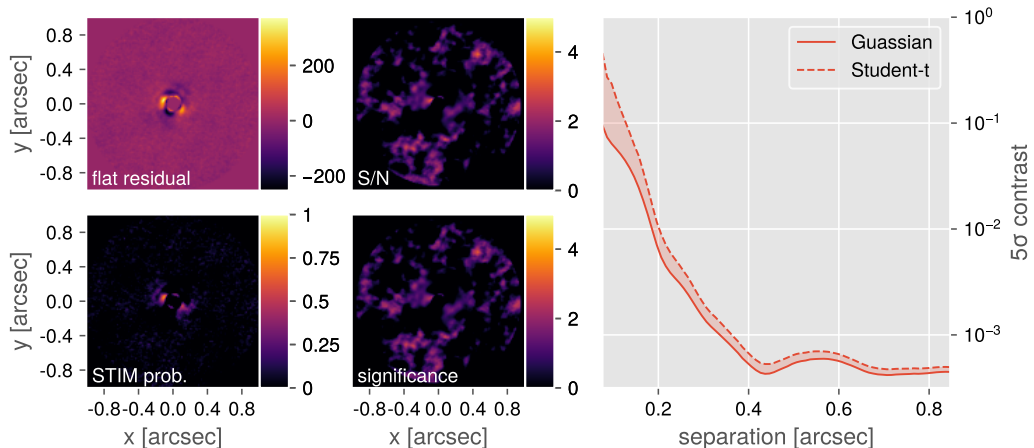


Figure 17. 2020-11-21 NMF subtraction with 2 components.

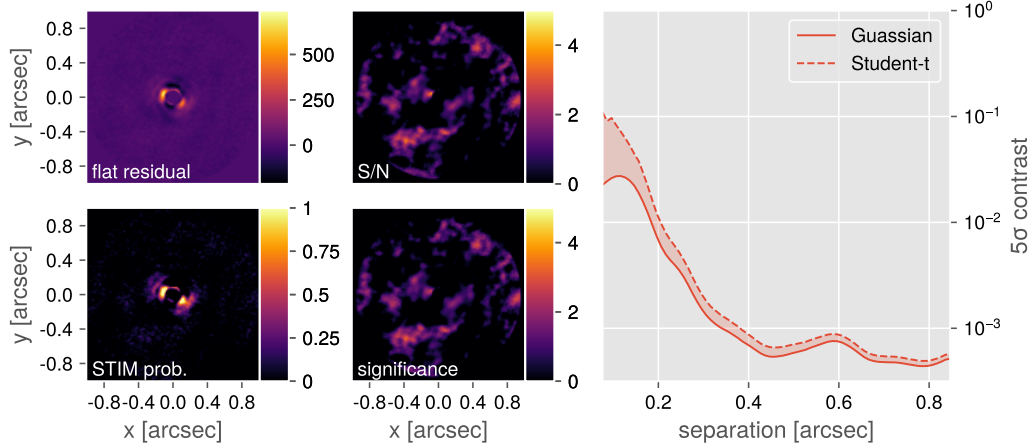


Figure 18. 2020-11-21 GreeDS with 2 components.

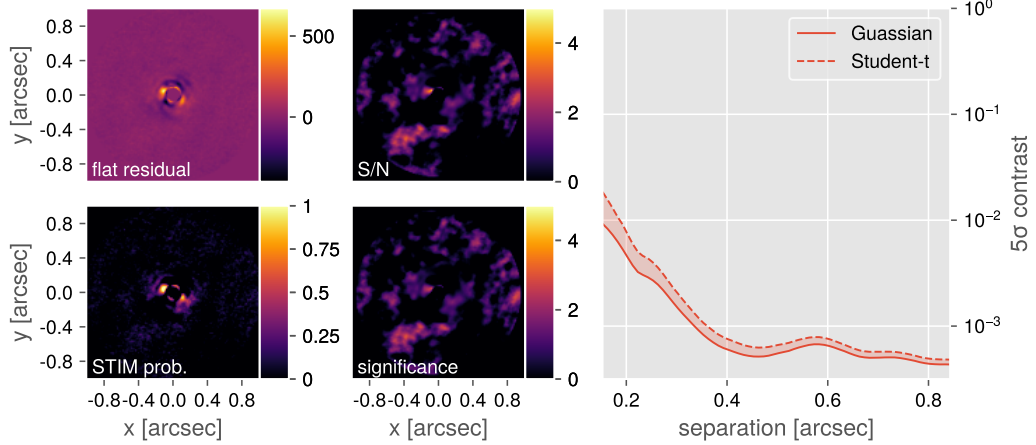


Figure 19. 2020-11-21 annular median subtraction with a rotation threshold of 0.5.

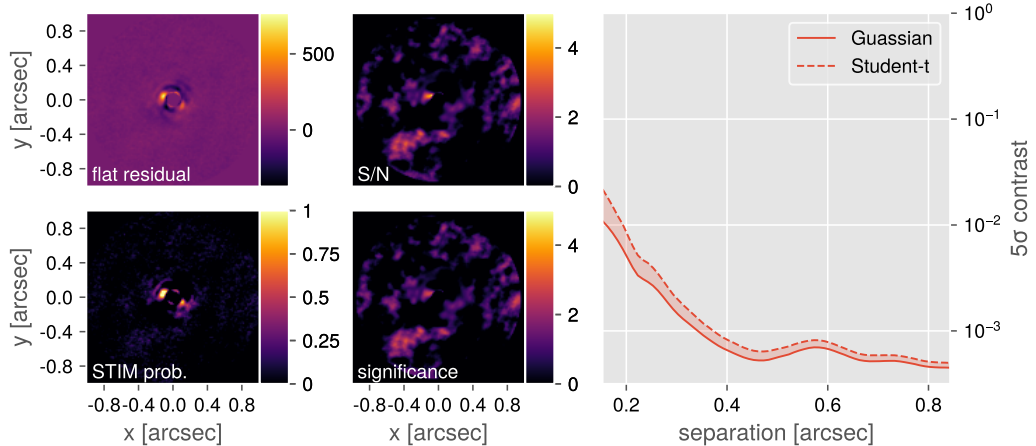


Figure 20. 2020-11-21 annular PCA subtraction with 2 components and a rotation threshold of nov21 0.5.

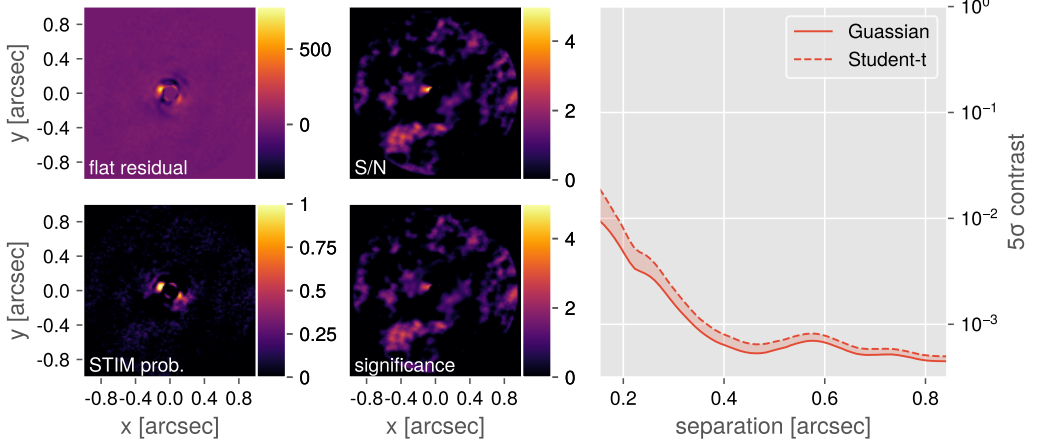


Figure 21. 2020-11-21 annular NMF subtraction with 2 components and a rotation threshold of 0.5.

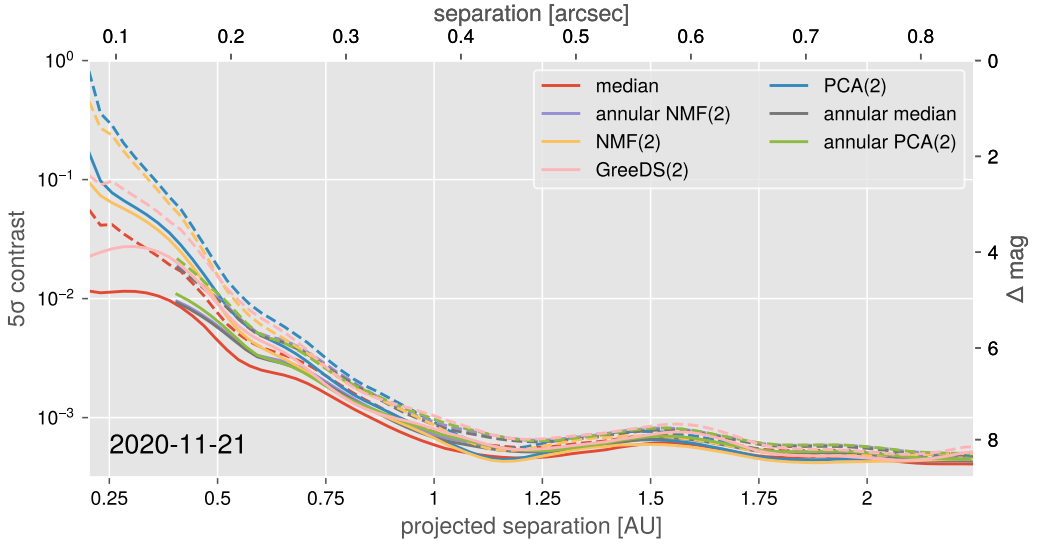


Figure 22. 5 σ contrast curves from various ADI algorithms for the 2020-11-21 epoch. Both the Gaussian (solid lines) and Student-t corrected (dashed lines) contrast curves are shown.

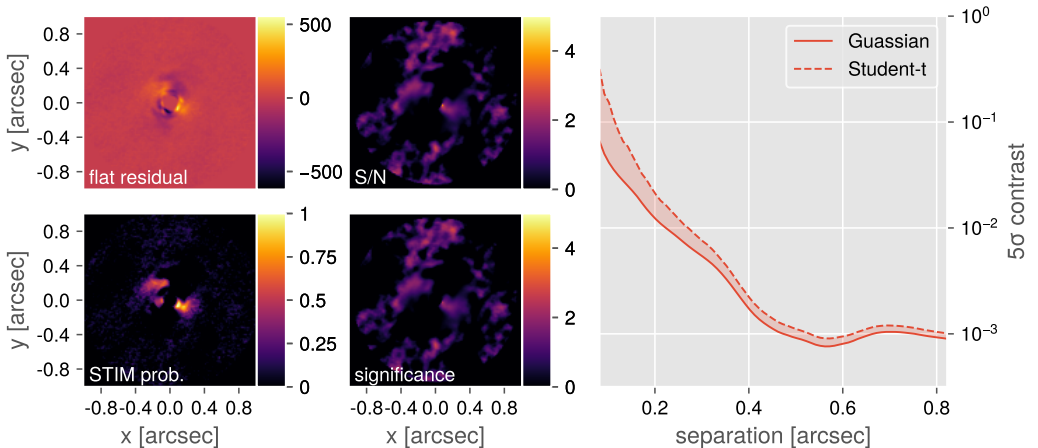


Figure 23. 2020-11-28 median subtraction.

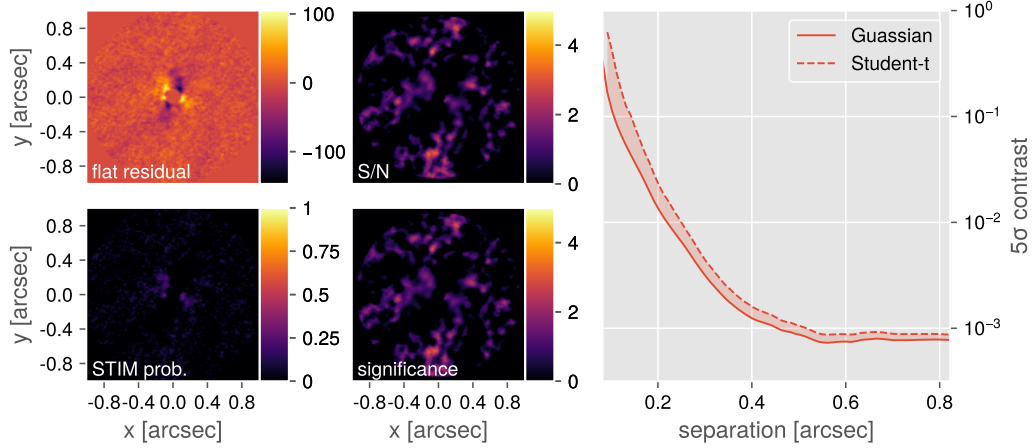


Figure 24. 2020-11-28 PCA subtraction with 2 components.

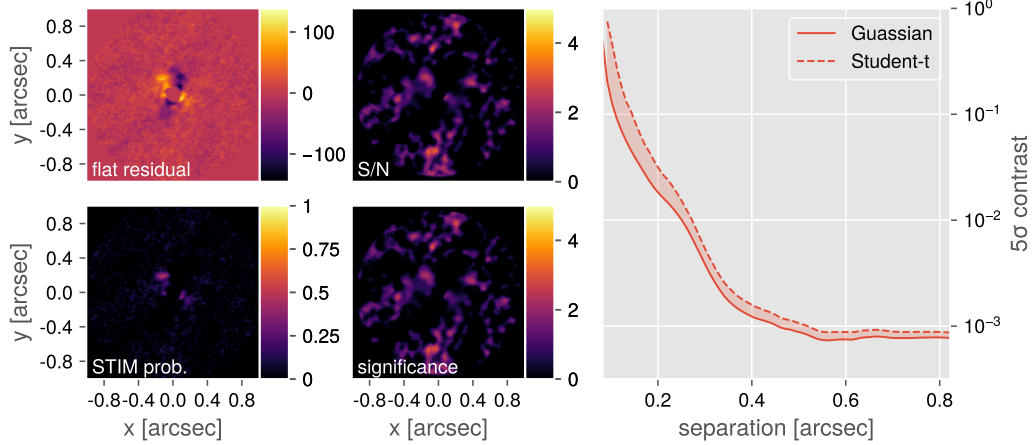


Figure 25. 2020-11-28 NMF subtraction with 2 components.

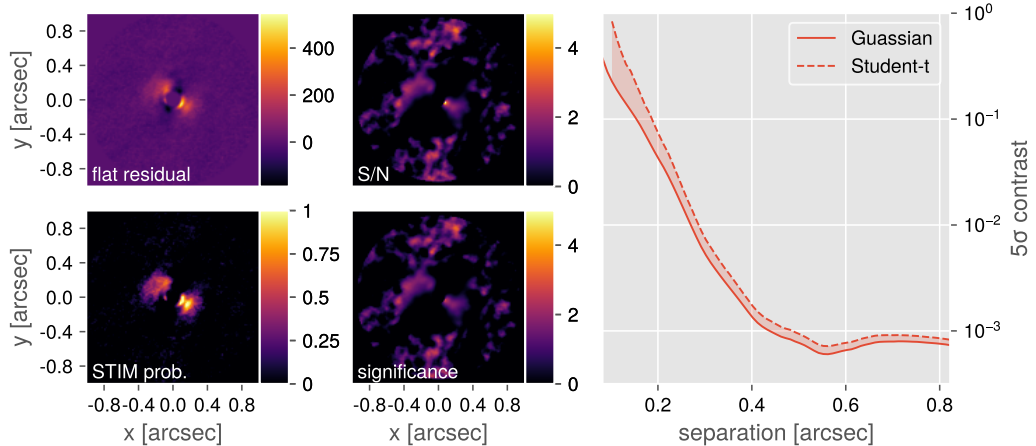


Figure 26. 2020-11-28 GreeDS with 2 components.

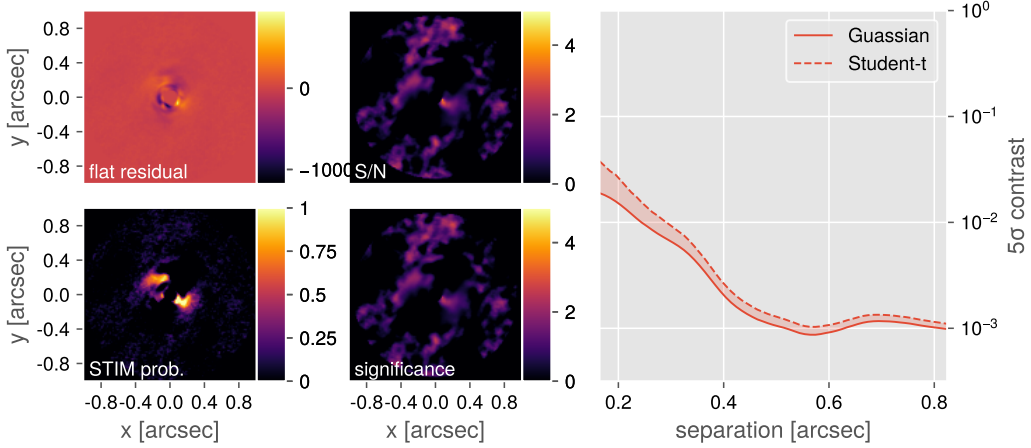


Figure 27. 2020-11-28 annular median subtraction with a rotation threshold of 0.5.

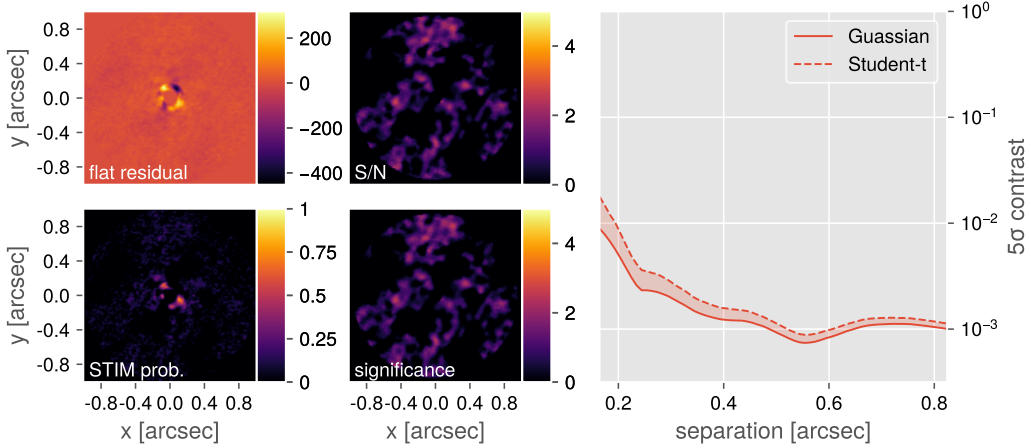


Figure 28. 2020-11-28 annular PCA subtraction with 2 components and a rotation threshold of nov28 0.5.

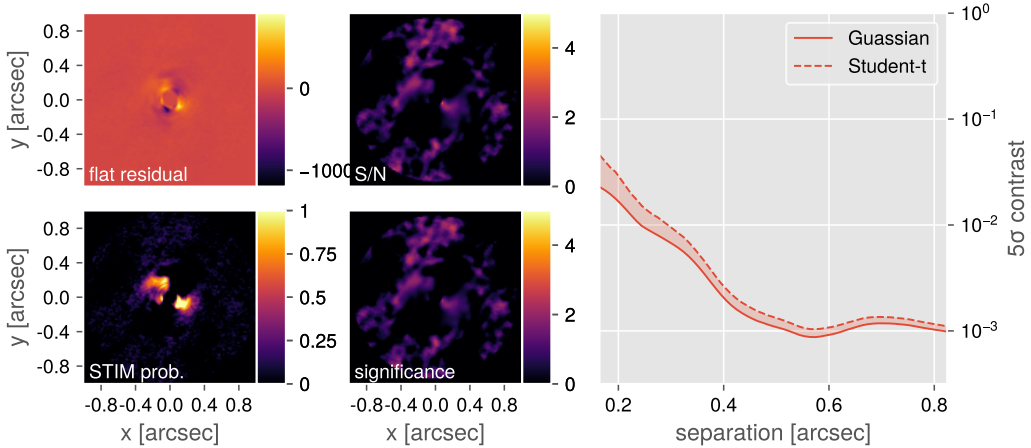


Figure 29. 2020-11-28 annular NMF subtraction with 2 components and a rotation threshold of 0.5.

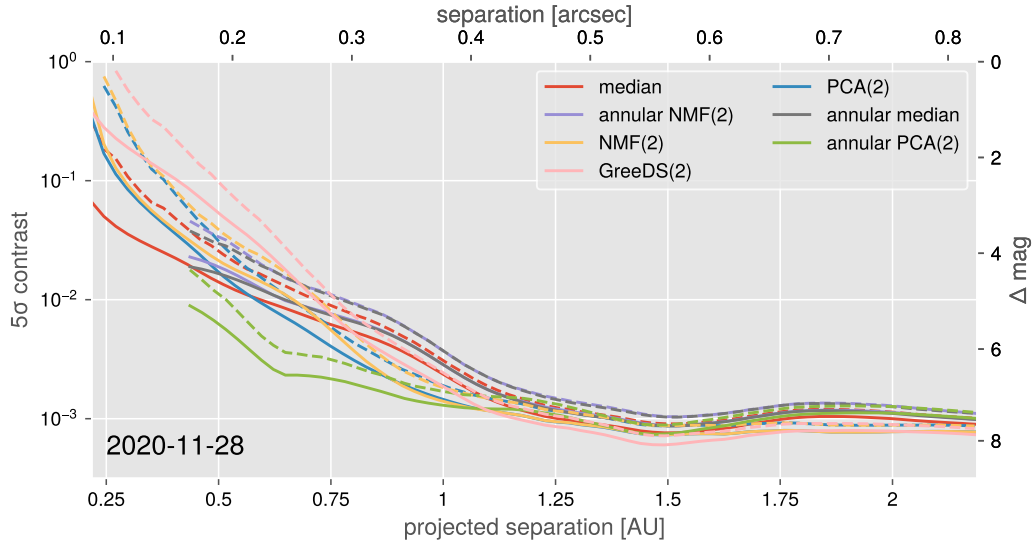


Figure 30. 5σ contrast curves from various ADI algorithms for the 2020-11-28 epoch. Both the Gaussian (solid lines) and Student-t corrected (dashed lines) contrast curves are shown.

B. PROVISIONAL ORBIT FITTING

Table 2. Provisional astrometry for blobs of interest from each epoch. The uncertainties are represented in parentheses and are derived from the FWHM of the PSF from each epoch.

| Date observed | offset (mas) | PA ($^{\circ}$) |
|---------------|--------------|-------------------|
| 2020-02-04 | 114 ± 40 | -115 ± 20 |
| 2020-11-21 | 121 ± 38 | -119 ± 18 |
| 2020-11-28 | 114 ± 41 | -113 ± 21 |

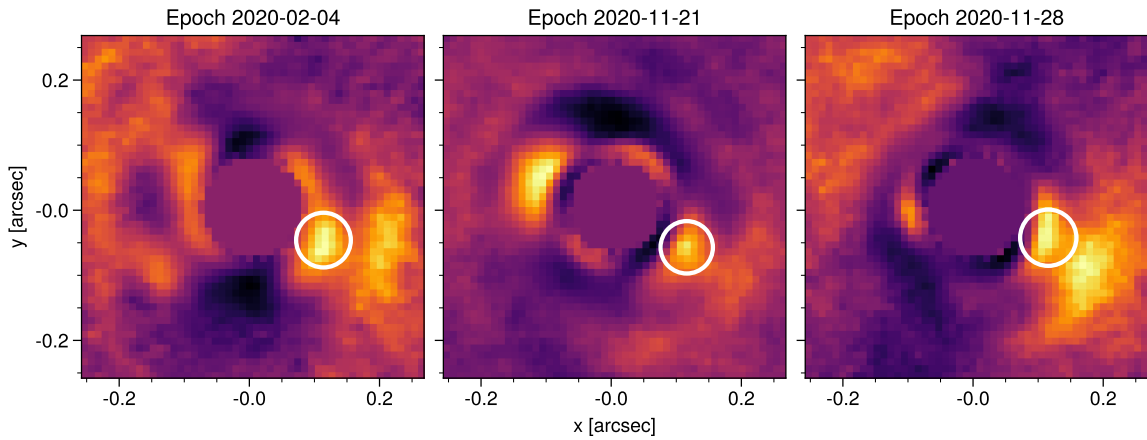


Figure 31. Provisional astrometry (white circles) displayed on STIM maps using the GreeDS algorithm with 2 components. Each frame was cropped to the inner $0.25''$ and the inner FWHM has been masked out. The width of the circles represent the uncertainty.

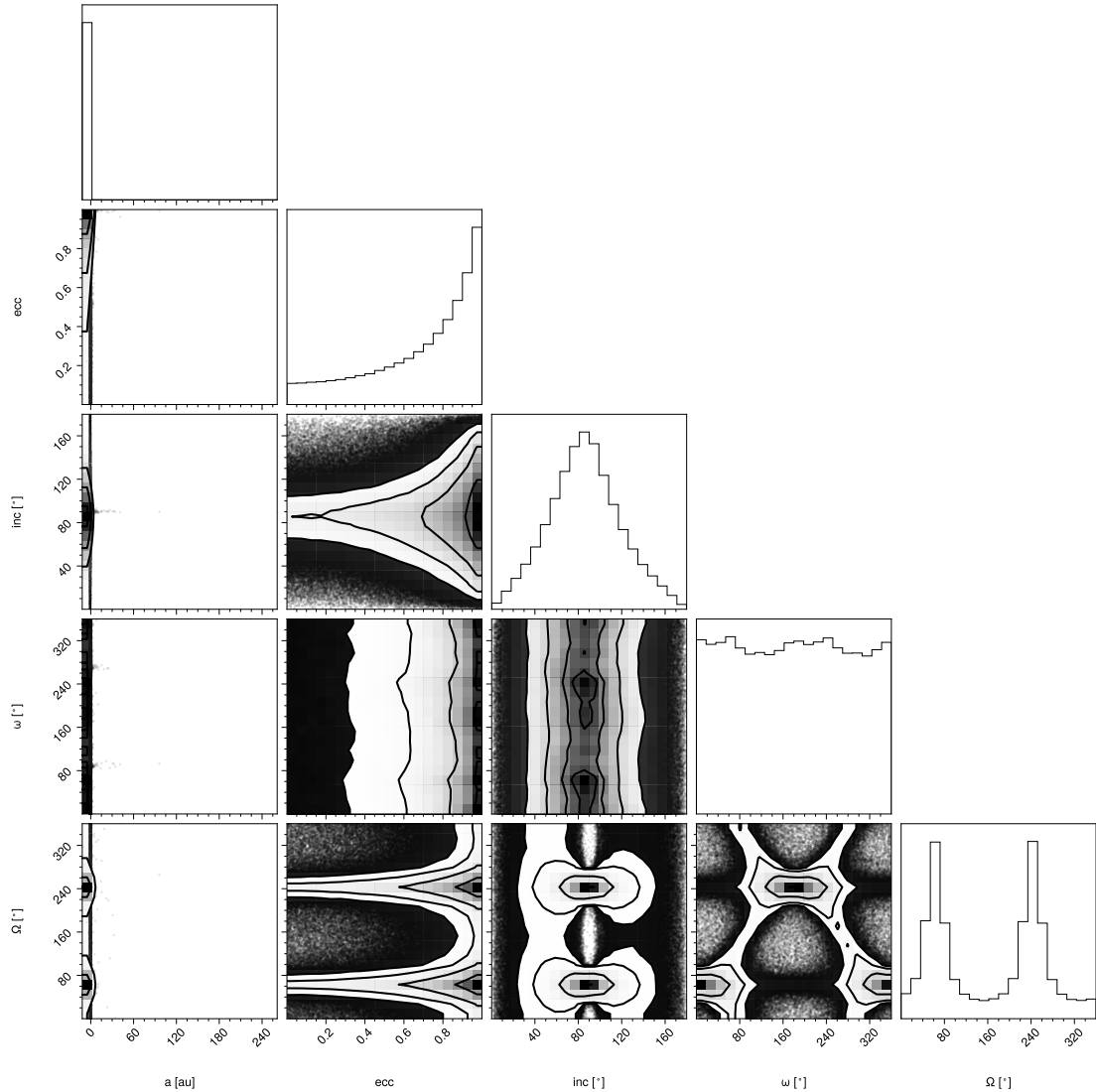


Figure 32. Corner plot of the marginal posteriors from the OFTI samples.